

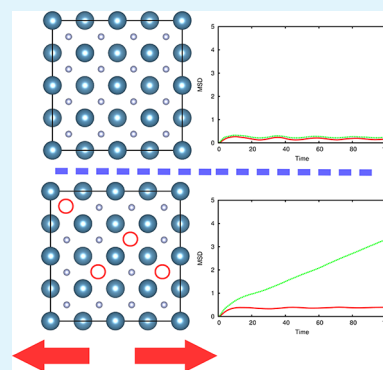
# Stress-Mediated Enhancement of Ionic Conductivity in Fast-Ion Conductors

Arun K. Sagotra and Claudio Cazorla\*School of Materials Science and Engineering, UNSW Sydney, Sydney, NSW 2052, Australia  
Integrated Materials Design Centre, UNSW Sydney, Sydney, NSW 2052, Australia

## Supporting Information

**ABSTRACT:** Finding solid-state electrolytes with high ionic conductivity near room temperature is an important prerequisite for developing all-solid-state electrochemical batteries. Here, we investigate the effects of point defects (vacancies) and biaxial stress on the superionic properties of fast-ion conductors (represented by the archetypal compounds  $\text{CaF}_2$ , Li-rich antiperovskite  $\text{Li}_3\text{OCl}$ , and  $\text{AgI}$ ) by using classical molecular dynamics and first-principles simulation methods. We find that the critical superionic temperature of all analyzed families of fast-ion conductors can be reduced by several hundreds of degrees through the application of relatively small biaxial stresses ( $|\sigma| \leq 1$  GPa) on slightly defective samples ( $c_v \sim 1\%$ ). In  $\text{AgI}$ , we show that superionicity can be triggered at room temperature by applying a moderate compressive biaxial stress of  $\sim 1$  GPa. In this case, we reveal the existence of a  $\sigma$ -induced order–disorder phase transition involving sizable displacements of all the ions with respect to the equilibrium lattice that occurs prior to the stabilization of the superionic state. In  $\text{CaF}_2$  and  $\text{Li}_3\text{OCl}$ , by contrast, we find that tensile biaxial stress ( $\sigma < 0$ ) favors ionic conductivity as due to an effective increase of the volume available to interstitial ions, which lowers the formation energy of Frenkel pair defects. Our findings provide valuable microscopic insight into the behavior of fast-ion conductors under mechanical constraints, showing that biaxial stress (or, conversely, epitaxial strain) can be used as an effective means to enhance ionic conductivity.

**KEYWORDS:** fast-ion conductors, strain engineering, vacancies, density functional theory, molecular dynamics



## 1. INTRODUCTION

Fast-ion conductors (FIC) are materials that exhibit high ionic conductivity in the crystal phase.<sup>1</sup> Examples of FIC, also known as superionic conductors, include alkali-earth metal fluorides ( $\text{CaF}_2$ ), oxides (doped  $\text{CeO}_2$ ), and lithium-rich ( $\text{Li}_{10}\text{GeP}_2\text{S}_{12}$ ) compounds.<sup>1–3</sup> Fast-ion conductors offer the possibility of manufacturing all-solid-state electrochemical batteries via replacement of customary liquid electrolytes. All-solid state electrochemical batteries display a series of improvements with respect to standard batteries in terms of safety (superior thermal and mechanical stability), cyclability, and electrochemical performance.<sup>4,5</sup> FIC also are promising for solid-state cooling due to the high entropy change associated with their superionic phase transition, which can be controlled with external fields.<sup>6,7</sup> Nevertheless, most FIC present rather low ionic conductivities at room temperature, which hinders their use in practical applications. Consequently, intense research efforts are being focused on the enhancement of atomic diffusivity in superionic materials, primarily based on chemical and nanostructuring strategies.<sup>8–12</sup>

Biaxial stress (or, conversely, epitaxial strain) has emerged as a promising route for tuning of ionic transport in FIC. Essentially, the distances between the atoms can be altered through the application of mechanical stress, and this has a dramatic effect on the kinetic barriers and formation energy of defects governing ion migration.<sup>7,13</sup> For instance, an increase of

8 orders of magnitude in ionic conductivity has been measured in yttria stabilized zirconia as a result of a 7% lattice strain.<sup>10,14</sup> Also, a large room-temperature 50-fold increase in  $\text{Li}^+$  ion conductivity was predicted for highly strained  $\text{LiFePO}_4$ .<sup>15</sup> In practice, biaxial stresses, either of compressive ( $\sigma > 0$ ) or tensile ( $\sigma < 0$ ) type, can be realized in thin films (see, for instance, works 16–18) and are present in most electrolyte–electrode interfaces.<sup>19,20</sup> Meanwhile, thin film and two-dimensional solid-state batteries are highly desirable for portable-device applications (e.g., mobile phones, computers, and smart gadgets) as due to their high volumetric energy density and suitability to be fabricated into different scales and shapes.<sup>21</sup> However, a quantitative understanding of how biaxial stress directly correlates with ionic conductivity still is lacking. Nanostructured FIC normally contain a large concentration of crystalline defects (vacancies and dislocations) and interfaces (grain boundaries and interlayer regions in heterostructures), which critically affects ionic transport.<sup>9,10,22–24</sup> As a consequence, it is difficult, if not impossible, to disentangle the fundamental contributions from biaxial stress to ionic conductivity directly from the experiments.<sup>25,26</sup>

Received: August 5, 2017

Accepted: October 16, 2017

Published: October 16, 2017

Here, we use classical molecular dynamics and first-principles simulation methods to fill this knowledge gap. In particular, we analyze the effects of ionic vacancies and biaxial stress, both separately and jointly, on the ionic transport properties of three well-known families of FIC materials represented by  $\text{CaF}_2$ ,  $\text{Li}_3\text{OCl}$ , and  $\text{AgI}$ .<sup>1</sup> We show that the superionic transition temperature of all investigated FIC can be reduced by several hundreds of degrees via the application of relatively small biaxial stresses ( $|\sigma| \leq 1$  GPa) on systems containing tiny concentrations of vacancies ( $c_v \sim 1\%$ ). Depending on the material and nature of the superionic transformation, either tensile or compressive stress turns out to be most favorable for the enhancement of ionic conductivity. Thus, our work provides a basis for the rational design of improved solid electrolytes and caloric materials based on room-temperature fast-ion conductors.

## 2. SIMULATION METHODS

Biaxial stress conditions, namely,  $\sigma_{xx} = \sigma_{yy}$  and  $\sigma_{zz} = 0$ , were simulated using thermostatting and barostatting techniques when considering  $T \neq 0$  conditions or by fixing the orientation and length of two (out of the three) lattice vectors of the crystal primitive cell when considering  $T = 0$  conditions. In all the cases, periodic boundary conditions were applied along the three Cartesian directions; hence, the simulated single crystals were totally free of any surfaces or interfaces. We note that epitaxial strain is quantitatively defined as  $\eta(\sigma) = \frac{a(\sigma) - a_0}{a_0}$ , where  $a$  is the lattice parameter of the strained crystal within the  $x$ - $y$  plane and  $a_0$  the corresponding equilibrium lattice parameter (that is, obtained at  $\sigma = 0$  conditions).

**2.1. Classical Molecular Dynamics.** Molecular dynamics (MD) simulations were performed in the  $(N, P, T)$  ensemble with the LAMMPS code.<sup>27</sup> The pressure and temperature of the system were kept fluctuating around a set-point value using thermostatting and barostatting techniques, in which some dynamical variables are coupled to the particle velocities and simulation box dimensions. The interactions between atoms were modeled with rigid-ion potentials. We employed large simulation boxes, typically containing up to 8000 atoms, and applied periodic boundary conditions along the three Cartesian directions. Defective systems were generated by removing randomly a particular number of cations and anions from the system to maintain the condition of charge neutrality (hereafter,  $c_v$  refers to the concentration of vacancies involving mobile ions only). Newton's equations of motion were integrated using the customary Verlet's algorithm with a time-step length of  $10^{-3}$  ps. The typical duration of a MD run was 100 ps. A particle-particle particle-mesh  $k$ -space solver was used to compute long-range van der Waals and Coulomb interactions beyond a cutoff distance of 12 Å at each time step. We explicitly checked that by creating point defects in an ordered manner and/or by increasing the total duration of the simulations up to 500 ps, our results remained invariant within the statistical uncertainties (see Supporting Information).

The interatomic potentials that we adopted to investigate  $\text{CaF}_2$  and  $\text{Li}_3\text{OCl}$  with molecular dynamics simulations were of the Born–Mayer–Huggins form:

$$V_{ij}(r) = A_{ij}e^{-r/\rho_{ij}} - \frac{C_{ij}}{r^6} + \frac{Z_i Z_j}{r} \quad (1)$$

where subscripts  $i$  and  $j$  represent the ionic species in the system and  $r$  represents the radial distance between a couple of atoms; the corresponding parameter values are reported in Table 1.<sup>7,28–30</sup> Each pairwise interatomic term is composed of three different contributions: the first one is of exponential type and accounts for the short-ranged atomic repulsion deriving from the overlapping between electron clouds; the second term is proportional to  $r^{-6}$  and represents the long-ranged atomic attraction due to dispersive van der Waals forces, and

**Table 1. Interatomic Potential Parameters Used to Describe  $\text{CaF}_2$ <sup>7,28</sup> and  $\text{Li}_3\text{OCl}$ <sup>29,30</sup> in Our Classical Molecular Dynamics Simulations<sup>a</sup>**

	A (eV)	$\rho$ (Å)	C (eV Å <sup>6</sup> )
<b>CaF<sub>2</sub></b>			
Ca <sup>+</sup> –F <sup>–</sup>	1717.441	0.287	0.102
F <sup>–</sup> –F <sup>–</sup>	2058.994	0.252	16.703
Ca <sup>+</sup> –Ca <sup>+</sup>	0.0	0.0	0.0
<b>Li<sub>3</sub>OCl</b>			
O <sup>2–</sup> –O <sup>2–</sup>	22764.30	0.1490	13.185
Cl <sup>–</sup> –Cl <sup>–</sup>	5145.28	0.3066	20.523
Li <sup>+</sup> –O <sup>2–</sup>	433.26	0.3138	0.0
Li <sup>+</sup> –Cl <sup>–</sup>	421.04	0.3364	0.0
Li <sup>+</sup> –Li <sup>+</sup>	360.53	0.1609	0.0

<sup>a</sup>Ionic charges are  $Z_{\text{Ca}} = 2$ ,  $Z_{\text{F}} = -1$ ,  $Z_{\text{Li}} = 1$ ,  $Z_{\text{O}} = -2$ , and  $Z_{\text{Cl}} = -1$ , as expressed in units of  $e$ .

the third term is the usual Coulomb interaction between point atomic charges.

The interatomic potential that we used to investigate  $\text{AgI}$  with molecular dynamics simulations is that due to Vashishta and Rahman,<sup>31</sup> which is expressed as

$$U_{ij}(r) = \frac{H_{ij}}{r^{n_{ij}}} - \frac{W_{ij}}{r^6} + \frac{Z_i Z_j}{r} - \frac{P_{ij}}{r^4} \quad (2)$$

where again subscripts  $i$  and  $j$  represent the ionic species in the system and  $r$  represents the radial distance between a couple of atoms; the corresponding parameter values are reported in Table 2. In this case,

**Table 2. Interatomic Potential Parameters Used to Describe  $\text{AgI}$ <sup>31</sup> in Our Classical Molecular Dynamics Simulations<sup>a</sup>**

$Z_{\text{Ag}}$	+0.6	$H_{\text{I–I}}$	6427.1
$Z_{\text{I}}$	–0.6	$P_{\text{Ag–Ag}}$	0.0
$n_{\text{Ag–Ag}}$	11	$P_{\text{Ag–I}}$	16.888
$n_{\text{Ag–I}}$	9	$P_{\text{I–I}}$	33.776
$n_{\text{I–I}}$	7	$W_{\text{Ag–Ag}}$	0.0
$H_{\text{Ag–Ag}}$	0.213	$W_{\text{Ag–I}}$	0.0
$H_{\text{Ag–I}}$	1647.4	$W_{\text{I–I}}$	99.767

<sup>a</sup>Ionic charges, distances, and energies are expressed in units of  $e$ , Å, and eV, respectively.

each pairwise interatomic term is composed of four different contributions; the first three terms in eq 2 are physically equivalent to those found in eq 1, with the only difference that the short-ranged repulsion between ions now is modeled with a negative power law. A fourth attractive contribution to the interaction energy is added that accounts for the effects of the electronic polarizabilities.

To analyze the superionic transport properties of fast-ion conductors, we computed the corresponding diffusion coefficient,  $D$ , and mean squared displacement (MSD), as extensively done in previous studies.<sup>7,13,32,33</sup> The diffusion coefficient is defined as

$$D = \lim_{t \rightarrow \infty} \left[ \frac{1}{2dt} \langle \Delta R_i^2(t) \rangle \right] \quad (3)$$

where  $d$  is the dimension of the lattice in which ion hopping occurs (e.g.,  $d = 3$  in the present case). At the same time, the MSD is defined as

$$\langle \Delta R_i^2(t) \rangle = \langle [\mathbf{r}_i(t + t_0) - \mathbf{r}_i(t_0)]^2 \rangle \quad (4)$$

where  $\mathbf{r}_i(t)$  is the position of the  $i$ th atom at time  $t$ ,  $t_0$  is an arbitrary time origin, and  $\langle \dots \rangle$  denotes average over time, time origins, and ions belonging to a same species. In practice,  $D$  is estimated by performing linear fits to the MSD data generated at long simulation times.

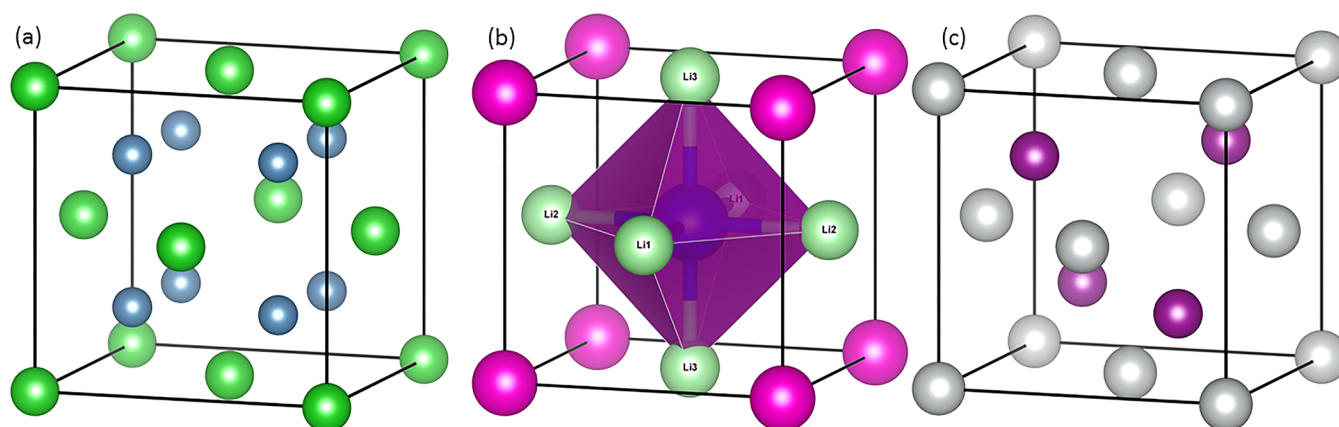


**Figure 1.** Sketch of the analyzed compounds and corresponding atomic structures. (a)  $\text{CaF}_2$  in the cubic fluorite structure; Ca and F ions are represented with green and blue spheres, respectively. (b)  $\text{Li}_3\text{OCl}$  in the cubic antiperovskite structure; Li, O, and Cl ions are represented with green, magenta, and blue spheres, respectively. (c)  $\text{AgI}$  in the cubic zincblende structure; Ag and I ions are represented with gray and purple spheres, respectively.

**2.2. Density Functional Theory.** First-principles calculations based on density functional theory (DFT) were carried out to analyze the energy and structural properties of  $\text{CaF}_2$ ,  $\text{Li}_3\text{OCl}$ , and  $\text{AgI}$  systems at zero temperature. We performed these calculations with the VASP code<sup>34</sup> by following the generalized gradient approximation to the exchange–correlation energy due to Perdew et al.<sup>35</sup> The projector augmented wave method was used to represent the ionic cores;<sup>36</sup> the following electronic states were considered as valence:  $2s\text{--}3s\text{--}3p\text{--}4s$  of Ca,  $2s\text{--}2p$  of F,  $1s\text{--}2s$  of Li,  $2s\text{--}2p$  of O,  $2s\text{--}2p$  of Cl,  $4d\text{--}5s$  of Ag, and  $5s\text{--}5p$  of I atoms. Wave functions were represented in a plane-wave basis truncated at 650 eV. By using these parameters and dense k-point grids for Brillouin zone integration, the resulting energies were converged to within 1 meV per formula unit (f.u.). In the zero-temperature geometry relaxations, an atomic force tolerance of  $0.01 \text{ eV}\cdot\text{\AA}^{-1}$  was imposed.

We also performed ab initio phonon frequency calculations with the direct method to assess the vibrational stability of the analyzed systems. In the direct method, the force–constant matrix is calculated in real-space by considering the proportionality between atomic displacements and forces.<sup>37–39</sup> The quantities with respect to which our phonon calculations were converged include the size of the supercell, the size of the atomic displacements, and the numerical accuracy in the sampling of the Brillouin zone. We found the following settings to provide quasi-harmonic free energies converged to within 5 meV per formula unit:<sup>39</sup>  $3 \times 3 \times 3$  supercells (where the figures indicate the number of replicas of the unit cell along the corresponding lattice vectors), atomic displacements of  $0.02 \text{ \AA}$ , and q-point grids of  $14 \times 14 \times 14$ . The values of the phonon frequencies were obtained with the PHON code developed by Alfè.<sup>38</sup> In using this code, we exploited the translational invariance of the system to impose the three acoustic branches to be exactly zero at the center of the Brillouin zone and applied central differences in the atomic forces.

We also performed  $(N, V, T)$  ab initio molecular dynamics (AIMD) simulations for bulk  $\text{CaF}_2$  (perfect and with vacancies),  $\text{Li}_3\text{OCl}$  (perfect and with vacancies), and  $\text{AgI}$  (perfect). The objective of these calculations was to assess the reliability of the interatomic potential models employed in our classical MD simulations. The temperature in our AIMD simulations was kept fluctuating around a set-point value by using Nose–Hoover thermostats. Simulation boxes containing up to 192 atoms were used in all the cases, and periodic boundary conditions were applied along the three Cartesian directions. Newton's equations of motion were integrated using the customary Verlet's algorithm and a time-step length of  $10^{-3}$  ps. We employed  $\Gamma$ -point sampling for integration within the first Brillouin zone. The duration of a typical AIMD was  $\sim 30$  ps. We focused on the analysis of the superionic features, which consistently are identified via inspection of the MSD profiles obtained in the AIMD simulations.

**2.3. Tests of the Interatomic Potentials.** In two previous works,<sup>7,28</sup> we already validated the reliability of the  $\text{CaF}_2$  interatomic potential employed to describe perfect systems ( $c_v = 0\%$ ) in our MD simulations. We carried out additional AIMD tests to check whether the same level of accuracy is maintained for defective systems. In particular, we performed classical and ab initio simulations for  $\text{CaF}_2$  crystals considering a concentration of vacancies of 5% and hydrostatic pressures of  $P = 0, 3,$  and  $5 \text{ GPa}$ . At those conditions, we obtain superionic transition temperatures of  $T_s^{\text{DFT}} = 900 (100), 1075 (100),$  and  $1000 (100) \text{ K}$  in the AIMD simulations, respectively, and of  $T_s^{\text{MD}} = 900 (50), 950 (50),$  and  $1000 (50) \text{ K}$  in the classical molecular dynamics simulations (statistical uncertainties are indicated within parentheses). Similarly, for  $c_v = 1\%$  and zero pressure, we find  $T_s^{\text{DFT}} = 1075 (100) \text{ K}$  and  $T_s^{\text{MD}} = 1100 (50) \text{ K}$ . Therefore, we conclude that the employed interaction potential model appears to be physically reliable for describing defective  $\text{CaF}_2$  systems as well, as it provides results that are consistent with first-principles methods.

Regarding  $\text{Li}_3\text{OCl}$ , we initially performed a series of both classical and ab initio simulations of the perfect system considering  $T \neq 0$  and zero-pressure conditions. In both cases, we consistently found that the crystal remained in the normal state all the way up to melting. Likewise, we simulated  $\text{Li}_3\text{OCl}$  with a concentration of vacancies of 1% at  $P = 0 \text{ GPa}$ . The superionic transition temperature obtained in this case with DFT methods was  $T_s^{\text{DFT}} = 1250 (100) \text{ K}$  and with classical molecular dynamics  $T_s^{\text{MD}} = 1160 (50) \text{ K}$ . Therefore, we conclude that the adopted  $\text{Li}_3\text{OCl}$  interaction potential model appears to be physically reliable, as it provides results that are consistent with first-principles methods.

It has been already demonstrated by others that the Vashishta–Rahman potential<sup>31</sup> mimics bulk  $\text{AgI}$  with great accuracy at  $T \neq 0$  conditions (see, for instance, works 40 and 41). Keen et al. observed a superionic transition under hydrostatic pressure in the rock-salt phase of bulk  $\text{AgI}$ .<sup>42</sup> The rock-salt structure consists of two interlaced fcc sublattices relatively displaced by  $(\frac{1}{2}, \frac{1}{2}, \frac{1}{2})$  in direct coordinates (space group  $Fm\bar{3}m$ ). We considered as a good test to check whether the Vashishta–Rahman potential could reproduce also the experimental findings obtained by Keen and collaborators. Our molecular dynamics simulations show that this is actually the case. In particular, we obtained a superionic transition temperature of  $450 (50) \text{ K}$  at  $P = 1 \text{ GPa}$  that compares very well with the experimental value of  $T_s^{\text{exp}} = 500 \text{ K}$ .<sup>42</sup> A similar good agreement was obtained also with respect to AIMD simulations performed under identical pressure conditions (i.e.,  $T_s^{\text{DFT}} = 435 (75) \text{ K}$ ). Therefore, we conclude that for present purposes, the Vashishta–Rahman potential represents a physically reliable interaction model, as it provides results that are consistent both with experiments and first-principles methods.

### 3. RESULTS AND DISCUSSION

**3.1. Type-II FIC: CaF<sub>2</sub>.** Type-II FIC present a continuous normal to superionic phase transition in which the symmetry of the sublattice formed by nondiffusive ions remains unchanged.<sup>1</sup> CaF<sub>2</sub> is an archetypal type-II FIC with a cubic fluorite structure (space group *Fm3m*) in which the Ca<sup>2+</sup> cations are arranged in a face-centered cubic lattice and the F<sup>-</sup> anions in a simple cubic lattice (see Figure 1a). Under biaxial stress, the cubic symmetry of the system is lifted, and CaF<sub>2</sub> adopts a tetragonal phase (space group *I4/mmm*). Figure 2 shows the total energy and

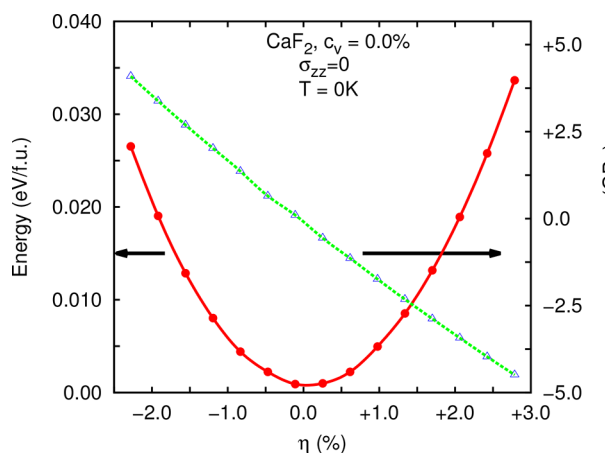


**Figure 2.** Energy and mechanical biaxial stress calculated in CaF<sub>2</sub> with DFT methods as a function of biaxial strain. Results are obtained for the perfect system at zero temperature, and the calculated equilibrium lattice parameter is  $a_0 = 5.50$  Å. Lines are guides to the eye.

biaxial stress calculated in perfect CaF<sub>2</sub> at zero temperature as a function of epitaxial strain; no solid–solid phase transition or vibrational instability (see Section 2.2) was found to occur within the investigated  $\eta$  interval.

As the temperature is increased beyond a certain critical point,  $T_s$ , the F<sup>-</sup> ions start to diffuse appreciably through the crystalline Ca<sup>2+</sup> matrix, and the system becomes superionic. In perfect ( $c_v = 0\%$ ) and unstrained CaF<sub>2</sub>, the superionic transition temperature amounts to 1400 (90) K<sup>13,28</sup> (see Figure 3). When vacancies are introduced in the crystal, the diffusivity of F<sup>-</sup> ions is greatly enhanced, even at temperatures well below the  $T_s$  corresponding to the perfect system (see Figure 4, where we compare the MSD profiles obtained in the  $c_v = 0$  and 2.5% cases). Consequently, discrimination between the normal and superionic states becomes further blurred. Here, we ascribe the superionic transition temperature of defective CaF<sub>2</sub> crystals (and also of defective Li<sub>3</sub>OCl and AgI, see the Supporting Information) to the temperature at which the corresponding diffusion coefficients match the  $D$  value estimated for the same transition in the equivalent perfect system (see Figure 3a); typical ionic conductivity values of  $\sim 10^{-4}$  S/cm are obtained at those transition points with the well-known Nernst–Einstein relationship.<sup>43</sup> In Figure 3b, we can appreciate the effects of  $c_v$  on the superionic transition temperature of unstrained CaF<sub>2</sub> (case  $\sigma = 0$ ). Essentially,  $T_s$  is reduced by  $\sim 200$  K when considering a relatively small vacancy concentration of 1%. The decrease in the critical superionic temperature, however, is not linear on  $c_v$ , as for a further  $T_s$  reduction of approximately 200 K is necessary to consider a defect concentration of 5%.

Figure 3b also shows the influence of biaxial stress on  $T_s$ . In the perfect crystal, we find that tensile stress systematically

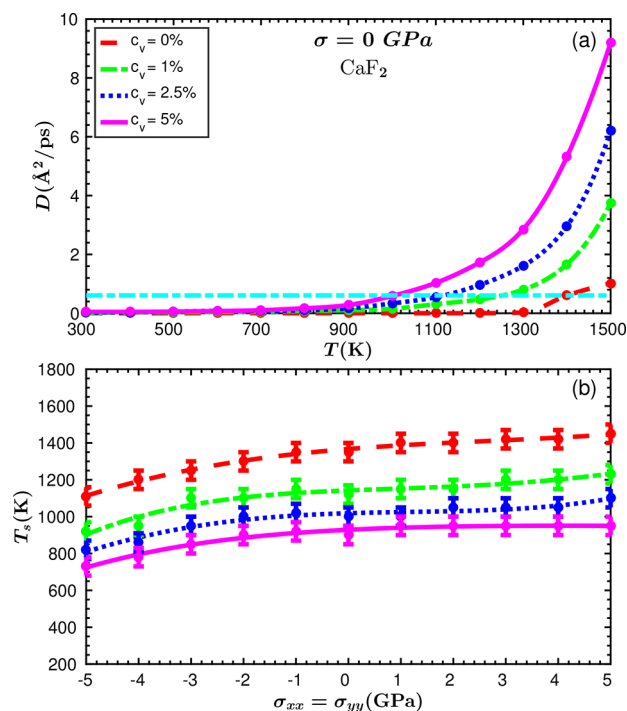


**Figure 3.** Superionic properties of CaF<sub>2</sub> calculated with MD methods as a function of vacancy concentration and biaxial stress. (a) Diffusion coefficient; the blue horizontal line indicates the value at which the perfect system becomes superionic in the absence of mechanical stresses. (b) Superionic transition temperature expressed as a function of  $c_v$  and  $\sigma$ . Lines are eye guides.

lowers the superionic transition temperature of the system, whereas compressive stress increases it. The variation of  $T_s$  in the  $\sigma < 0$  side is larger in absolute value than in the  $0 < \sigma$  side. For instance, at  $\sigma = -5$  GPa ( $\sigma = 5$  GPa) the superionic transition temperature of CaF<sub>2</sub> is reduced (increased) by  $\sim 200$  K ( $\sim 100$  K) with respect to the value obtained at zero-stress conditions. According to the results shown in Figure 2, a tensile biaxial stress of  $-5$  GPa may be achieved through an epitaxial lattice strain of  $\eta \sim 3\%$ ; these conditions could be realized in CaF<sub>2</sub> thin films grown on top of Ge or AlAs substrates (both with an equilibrium lattice parameter of 5.66 Å) because the equilibrium lattice parameter of bulk CaF<sub>2</sub> is 5.50 Å and all the named crystals possess cubic symmetry.

Why does tensile stress favors superionicity in type-II FIC? Upon application of a negative  $\sigma$ , the crystal expands along the Cartesian  $x$  and  $y$  directions and shrinks along  $z$  (as the Poisson's ratio of CaF<sub>2</sub> is positive). Consequently, the total volume of the system increases. Such a volume expansion, although is not isotropic, has the effect of lowering the formation energy of Frenkel pair defects (that is, the simultaneous formation of F<sup>-</sup> vacancy and interstitial pairs), which is the fundamental mechanism behind ionic conductivity in CaF<sub>2</sub>.<sup>44,45</sup> Conversely, compressive stress increases the formation energy of vacancy–interstitial pairs. Actually, at  $\sigma = -5$  GPa, the formation energy of Frenkel pair defects is found to be  $\sim 12\%$  smaller than the value obtained at equilibrium ( $\sim 2.0$  eV).<sup>7</sup> Meanwhile, in Figure S, we represent the ionic MSD calculated in superionic CaF<sub>2</sub> as a function of diffusion direction; from the slope of the two F<sup>-</sup> curves therein, it is appreciated that tensile stress slightly favors in-plane conductivity over out-of-plane conductivity, which appears to be

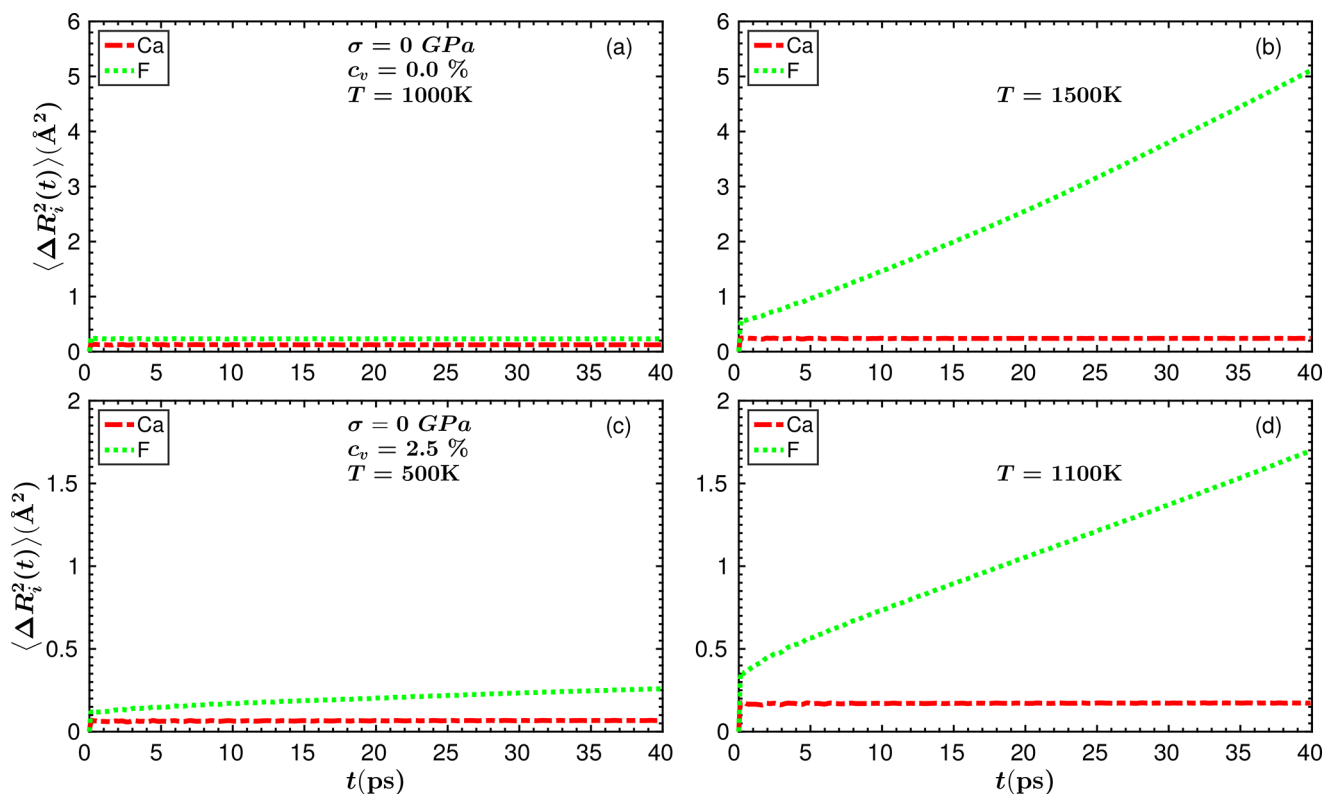


**Figure 4.** Mean squared displacement of unstrained  $\text{CaF}_2$  calculated with MD methods as a function of temperature and vacancy concentration. (a and b) Perfect system. (c and d) Defective system.

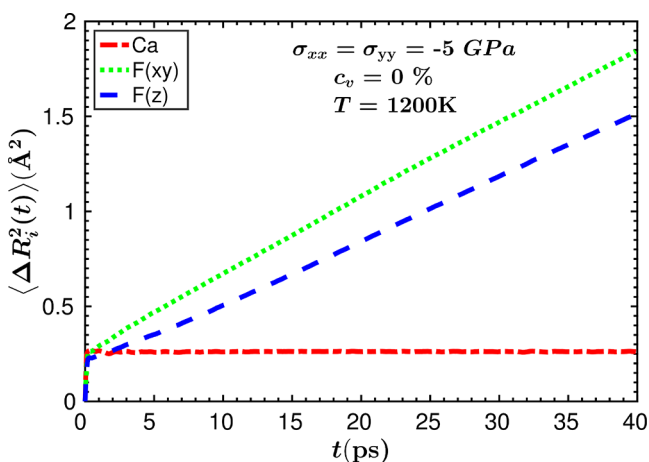


**Figure 5.** Mean squared displacement of strained  $\text{CaF}_2$  calculated with MD methods as a function  $\text{F}^-$  diffusion direction, that is, within the Cartesian  $x$ - $y$  plane or along the  $z$ -axis.

consistent with the anisotropic strain deformation experienced by the system.

When the effects of vacancies and tensile stress are considered together, the superionic transition temperature of  $\text{CaF}_2$  may undergo a reduction of several hundreds of degrees. For instance, for  $c_v = 1\%$  and  $\sigma = -5 \text{ GPa}$ , we obtain  $T_s = 900$  (50) K, which is about 500 K lower than the critical temperature estimated for the nondefective system at equilibrium (see Figure 3b). To obtain microscopic insight into the ion migration paths taking place in strained  $\text{CaF}_2$ , we analyzed the density distribution of  $\text{F}^-$  ions obtained at  $T \neq 0$  conditions. For this, we divided the system into a number of

slices of width  $\frac{1}{4}a$  along the out-of-plane  $z$  direction, and constructed  $x$ - $y$  fluorine position histograms by averaging the trajectories generated in our finite-temperature simulations (see Figure 6, where we enclose two representative density plots obtained for two consecutive system slices). In nondefective  $\text{CaF}_2$  under a biaxial tensile load of 4 GPa (Figures 6a and b),

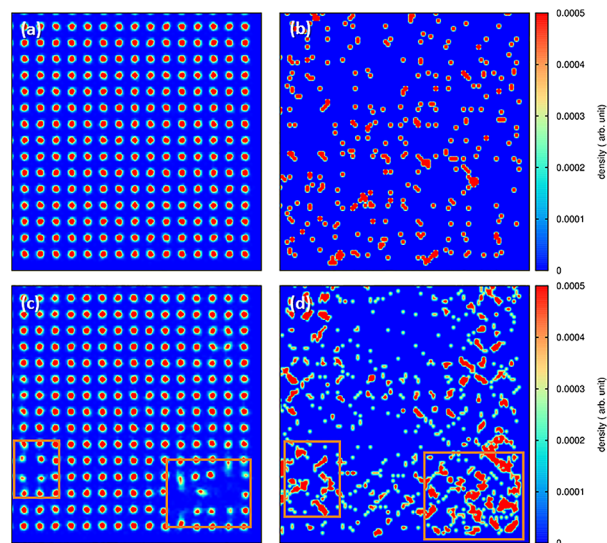


**Figure 6.** Fluorine density plots calculated in  $\text{CaF}_2$  with MD methods at  $\sigma_{xx} = \sigma_{yy} = -4 \text{ GPa}$  and  $T = 1200 \text{ K}$  conditions. (a and b) Perfect system. (c and d) Defective system ( $c_v = 2.5\%$ ); regions containing vacancies are highlighted with orange boxes. For clarity purposes, the positions of  $\text{Ca}^{2+}$  ions are not shown in the figure.

we find that the transport pathways of fluorine ions essentially are the same as those determined in the equivalent unstrained system. Specifically, the preferred positions for interstitial ions correspond to  $F(1) = (\frac{1}{2}, u, u)$  with  $u \sim 0.3$  and  $F(2) = (v, v, v)$  with  $v \sim 0.4$ , rather than to the more symmetric octahedral sites  $F(4) = (\frac{1}{2}, \frac{1}{2}, \frac{1}{2})$ <sup>46,47</sup> (see Supporting Information). In defective  $\text{CaF}_2$  ( $c_v = 2.5\%$ ) under a biaxial stress of  $\sigma = -4$  GPa, the voids introduced by the vacancies become preferential interstitial sites, in addition to positions  $F(1)$  and  $F(2)$ . This is clearly shown in Figures 6c and d, in which the larger concentrations of fluorine ions coincide with the regions accommodating point defects.

**3.2. Li-Rich Antiperovskite FIC:  $\text{Li}_3\text{OCl}$ .**  $\text{Li}_3\text{OCl}$  is a representative member of the family of Li-rich antiperovskite FIC.<sup>48</sup> This compound adopts a crystalline structure (space group  $Fm\bar{3}m$ ) characterized by Li, Cl, and O atoms resting on the octahedral vertices, octahedral centers, and center of a cubic unit cell, respectively (see Figure 1b). The primary mechanism for ion migration in  $\text{Li}_3\text{OCl}$  is related to the presence of vacancies and anion disorder; actually, in the absence of point defects, the diffusivity of  $\text{Li}^+$  ions is zero at temperatures below the corresponding melting point.<sup>29,49</sup> Under biaxial stress, the cubic symmetry of the system is lifted, and the crystal adopts a tetragonal phase (space group  $P4/mmm$ ). Figure 7 shows the

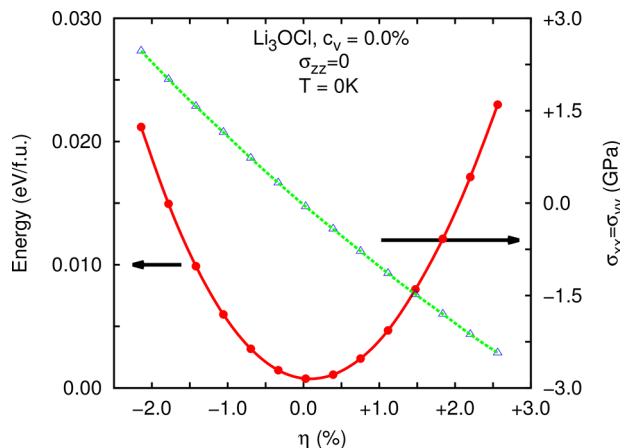


**Figure 7.** Energy and mechanical biaxial stress calculated in  $\text{Li}_3\text{OCl}$  with DFT methods as a function of biaxial strain. Results were obtained for the perfect system at zero temperature, and the calculated equilibrium lattice parameter is  $a_0 = 5.50$  Å. Lines are guides to the eye.

total energy and biaxial stress calculated in perfect  $\text{Li}_3\text{OCl}$  at zero temperature as a function of epitaxial strain; no solid–solid phase transition or vibrational instability (see Section 2.2) was found to occur within the investigated  $\eta$  interval.

Figure 8 shows the influence of vacancy concentration and biaxial stress on the superionic transition temperature of  $\text{Li}_3\text{OCl}$ . At  $\sigma = 0$  conditions, we obtain  $T_s = 1150$  (50) K for  $c_v = 1\%$  and  $T_s = 850$  (50) K for  $c_v = 5\%$ . In this case, the vacancy-induced enhancement of ionic conductivity is slightly inferior to that found in  $\text{CaF}_2$ . Analogously to what we have shown for type-II FIC, biaxial tensile stress induces a reduction of  $T_s$ , whereas compressive stress induces an increase. For instance, in the  $c_v = 1\%$  case, we find that at  $\sigma = -1.5$  GPa ( $\sigma = 1.5$  GPa), the superionic transition temperature decreases (increases) by  $\sim 125$  K ( $\sim 50$  K). (As it is shown in Figure 8, we obtain very

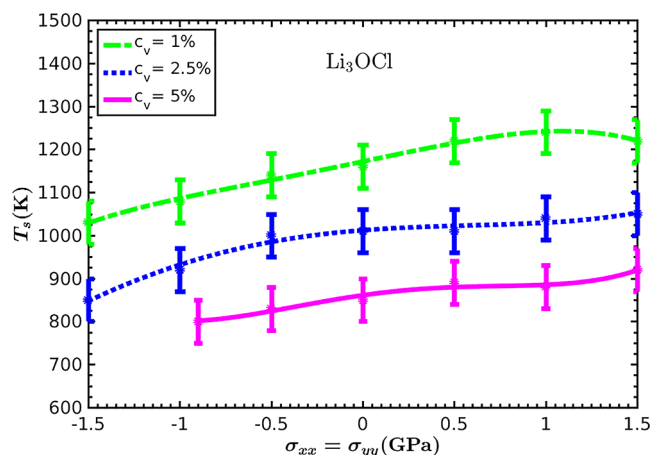


**Figure 8.** Critical superionic temperature of  $\text{Li}_3\text{OCl}$  calculated with MD methods and expressed as a function of biaxial stress and vacancy concentration. In the  $c_v = 5\%$  case, the system became unstable in our simulations at biaxial tensile stresses below approximately  $-1$  GPa. Lines are eye guides.

similar results in the rest of  $c_v$  cases.) The primary cause of such a  $T_s$  dependence on biaxial stress is the same than found in  $\text{CaF}_2$ , namely, the  $\sigma$ -induced variation of the formation energy of Frenkel pair defects (which intuitively can be understood in terms of the accompanying change of volume available to interstitial ions). In fact, we have calculated the formation energy of vacancy-interstitial pairs in perfect  $\text{Li}_3\text{OCl}$  with DFT methods along the guidelines explained in work;<sup>7</sup> at  $\sigma = -1.5$  GPa, we find a  $\sim 15\%$  reduction in the formation energy of Frenkel pair defects as compared to the equilibrium value ( $\sim 1.7$  eV), whereas at  $\sigma = 1.5$  GPa, the same quantity increases by  $\sim 12\%$ . According to the results shown in Figure 7, a tensile biaxial stress of  $-1.5$  GPa may be realized in  $\text{Li}_3\text{OCl}$  thin films with an epitaxial lattice strain of  $\eta \sim 1.5\%$  (where  $a_0 = 5.50$  Å).

From a crystal symmetry point of view, the three lithium atoms in the  $\text{Li}_3\text{OCl}$  unit cell rest either on apical (Li3 in Figure 1b) or equatorial (Li1 and Li2 in Figure 1b) positions. As it can be seen in Figure 9, equatorial  $\text{Li}^+$  ions contribute the most to ionic conductivity, as their diffusion coefficient is larger than that found for apical ions. To get microscopic insight into the ion migration paths taking place in strained  $\text{Li}_3\text{OCl}$ , we analyzed the density distribution of  $\text{Li}^+$  ions in a similar way as we did for  $\text{CaF}_2$  (see Section 3.1). In Figure 10, we show three representative ionic density plots obtained for three consecutive system partitions defined along the Cartesian  $z$  direction. Figure 10a contains a plane of equilibrium Li1 and Li2 positions, and Figure 10c contains a plane of equilibrium Li3 positions. We find that at  $\sigma = -1$  GPa, the diffusion of  $\text{Li}^+$  ions is greater within the Li–O planes (Figure 10a) than within the Li–Cl planes (Figure 10c), as shown by the fact that the voids introduced by equatorial vacancies are populated more appreciably than those introduced by apical vacancies. Meanwhile, high-density  $\text{Li}^+$  areas with cross shape appear in the region between Li–O and Li–Cl planes (see Figure 10b); these density patterns suggest that lithium ions preferably diffuse along the edges and faces of the  $\text{Li}_6$ -octahedra containing oxygen atoms in their interior (see Supporting Information). These results are consistent with the ion migration paths determined by other authors in unstrained  $\text{Li}_3\text{OCl}$ ,<sup>30</sup> hence corroborating the evidence that the origins of the revealed  $\sigma$ -

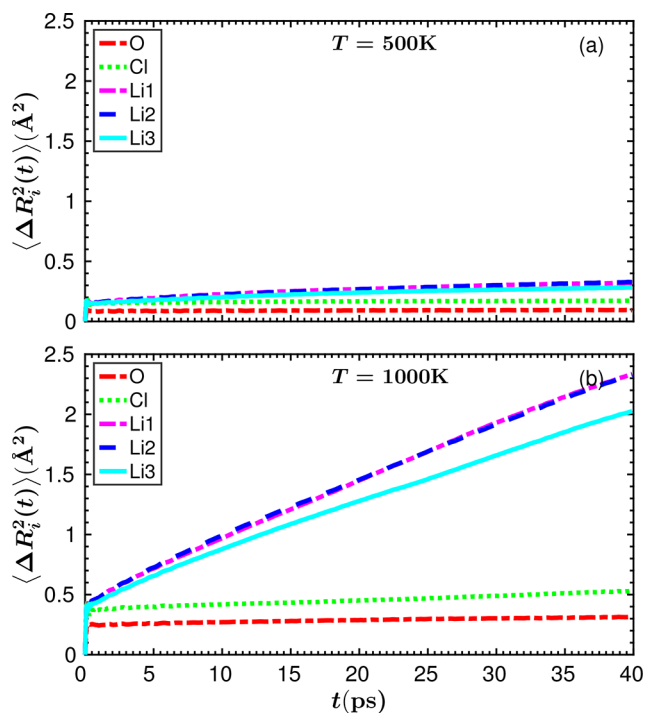


**Figure 9.** Mean squared displacement of  $\text{Li}_3\text{OCl}$  calculated with MD methods for a vacancy concentration of 2.5% and  $\sigma_{xx} = \sigma_{yy} = -1$  GPa, at  $T =$  (a) 500 and (b) 1000 K.

mediated enhancement of ionic conductivity essentially are of geometric nature.

We note that  $\text{Li}_3\text{OCl}$  behaves quite similarly to  $\text{CaF}_2$  in terms of enhancement of ionic conductivity under biaxial stress. Namely, biaxial tensile stress triggers a reduction of  $T_s$ , whereas compressive stress triggers an increase. Likewise, the superionic phase transition in  $\text{Li}_3\text{OCl}$  can be classified into type-II as it is continuous, and the symmetry of the sublattices formed by  $\text{Cl}^-$  and  $\text{O}^{2-}$  ions remain invariant during the phase transition. Therefore, we may generalize the result that biaxial tensile stress tends to favor ionic conductivity in families of type-II and alike FIC.

**3.3. Type-I FIC: AgI.** Type-I FIC presents an abrupt normal to superionic phase transition during which the symmetry of the sublattice formed by nondiffusive ions is transformed.<sup>1</sup> AgI

is an archetypal type-I FIC. At ambient conditions, bulk AgI is found as a mixture of wurtzite ( $\beta$ , hexagonal  $P6_3mc$ ) and zincblende ( $\gamma$ , cubic  $F43m$ ) phases.<sup>1</sup> As the temperature is increased beyond  $T_s \sim 420$  K, AgI transforms into a superionic phase ( $\alpha$ ) in which the  $\Gamma^-$  anions are rearranged into a cubic bcc lattice and the  $\text{Ag}^+$  cations become mobile. In practice, AgI thin films can be synthesized either in the  $\beta$  or  $\gamma$  phase depending on the employed preparation method.<sup>17,18</sup> For simplification purposes, here we consider the  $\gamma$  phase only, which consists of two interlaced monatomic fcc sublattices with fourfold ionic coordination. Under biaxial stress, the cubic symmetry of the system is lifted, and the crystal adopts a tetragonal phase (space group  $I4m2$ ). Figure 11 shows the total energy and biaxial stress

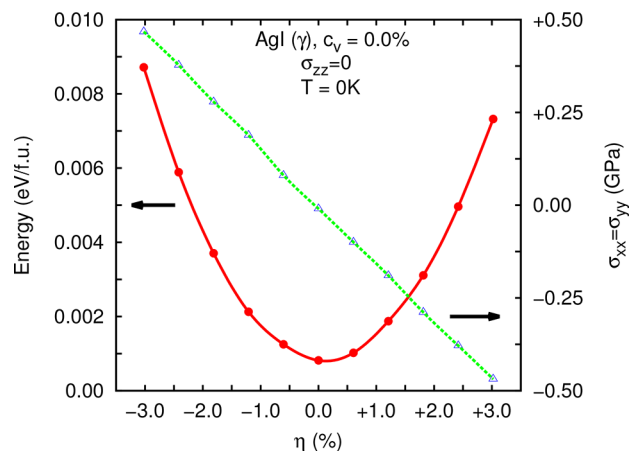


**Figure 11.** Energy and mechanical biaxial stress calculated in AgI with DFT methods as a function of biaxial strain. Results are obtained for the perfect system at zero temperature and the calculated equilibrium lattice parameter is  $a_0 = 6.62$  Å. Lines are guides to the eye.

calculated in perfect AgI at zero temperature as a function of epitaxial strain; no solid–solid phase transition or vibrational instability (see Section 2.2) was found to occur within the investigated  $\eta$  interval.

Figure 12 shows how biaxial compressive stress affects the superionic transition temperature of nondefective  $\gamma$ -AgI. (In our simulations, we observed that even small biaxial tensile stresses induced some mechanical instabilities in the system before becoming superionic, which precluded us from analyzing

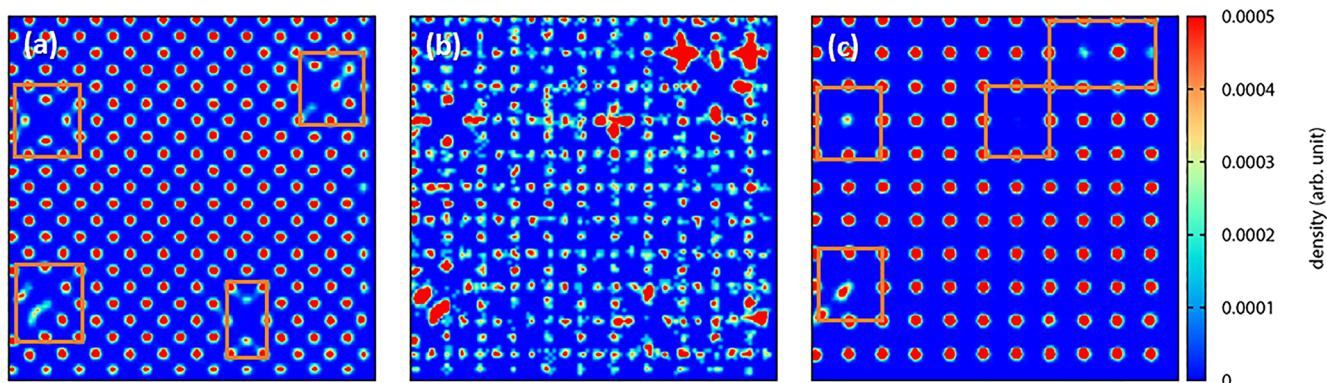


**Figure 10.** Lithium density plots calculated in  $\text{Li}_3\text{OCl}$  ( $c_v = 2.5\%$ ) with MD methods at  $\sigma_{xx} = \sigma_{yy} = -1$  GPa and  $T = 1000$  K conditions. (a) Thin slab containing Li1 and Li2 equilibrium positions (see text and Figure 1). (b) Thin slab between those containing Li1–Li2 and Li3 equilibrium positions (see text and Figure 1). (c) Thin slab containing Li3 equilibrium positions (see text and Figure 1). Regions containing vacancies are highlighted with orange boxes. For clarity purposes, the positions of  $\text{Cl}^-$  and  $\text{O}^{2-}$  ions are not shown.

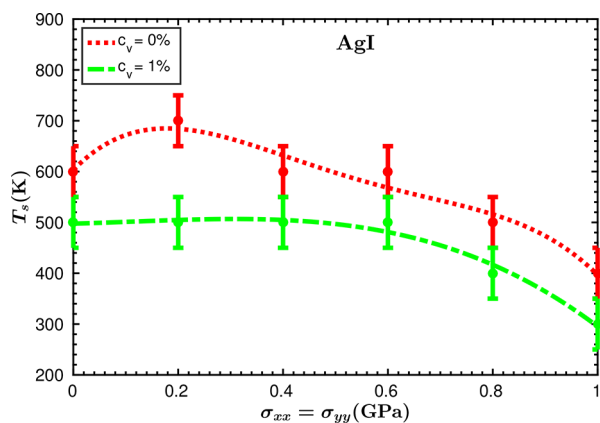


**Figure 12.** Critical superionic temperature of AgI ( $\gamma$  phase) calculated with MD methods and expressed as a function of biaxial stress and vacancy concentration. Lines are guides to the eye.

the normal superionic phase transition; consequently, we disregard  $\sigma < 0$  constraints in what follows.) It can be appreciated that  $T_s$  first increases under biaxial compressive stresses in the interval  $0 \leq \sigma \leq 0.2$  GPa [in particular,  $T_s$  changes from 600 (50) K at equilibrium to 700 (50) K at 0.2 GPa]. Subsequently, for  $\sigma \geq 0.2$  GPa, the superionic transition temperature decreases systematically and reaches, for instance, a value of 400 (50) K at 1 GPa. According to the results shown in Figure 11, a compressive biaxial stress of 0.2 GPa may be realized in AgI thin films with an epitaxial lattice strain of  $\eta \sim -2.8\%$  (where  $a_0 = 6.62$  Å). To shed light into the nonmonotonous  $T_s$  behavior found in  $\gamma$ -AgI, we analyzed thoroughly the ion transport and structural properties of the crystal at biaxial stresses above and below  $\sigma_c = 0.2$  GPa. Figure 13a shows the MSD of  $\text{Ag}^+$  and  $\text{I}^-$  ions calculated for a system without vacancies ( $c_v = 0\%$ ) at  $\sigma = 1$  GPa and  $T < T_s$ . The two ionic curves present an unusual shape in which the corresponding slopes are finite at short times and become zero at long times. At  $T = 400$  K (see Figure 13b), by contrast, only the  $\text{Ag}^+$  ions diffuse consistently through the system, and the usual superionic MSD profiles are rendered. These results appear to indicate the presence of some structural transformation in strained AgI before becoming superionic.

Our structural analysis based on the estimation of coordination numbers, radial pair distribution functions, and ionic density distributions actually reveals the existence of a  $\sigma$ -induced order–disorder phase transition in AgI affecting both  $\text{Ag}^+$  and  $\text{I}^-$  sublattices. In particular, the averaged I–I and Ag–Ag coordination numbers roughly amount to 12, similar to what is found in the two fcc sublattices integrating the parent  $\gamma$  phase, but the corresponding mean deviations are quite large, namely, of the order of 1 (we note that in the normal state the analogous coordination number mean deviations are of the order of 0.1, see Supporting Information). Likewise, a precise determination of neighboring atomic shells from the corresponding radial pair distribution functions,  $g(r)$ , is not possible at distances beyond few Angstroms when  $\sigma_c < \sigma$  (see Figure 14); by contrast, when biaxial stress is smaller than  $\sigma_c$  it is possible to identify up to three consecutive shells of neighboring atoms (not shown here). Furthermore, at  $T = 300$  K and  $\sigma = 1$  GPa, the asymptotic behavior of the ionic radial pair distribution functions, namely,  $g(r) \approx 1$  in the limit  $r \rightarrow \infty$ , is reached very rapidly with the radial distance ( $r \sim 12$  Å, see Figure 14). These results are consistent with a lack of

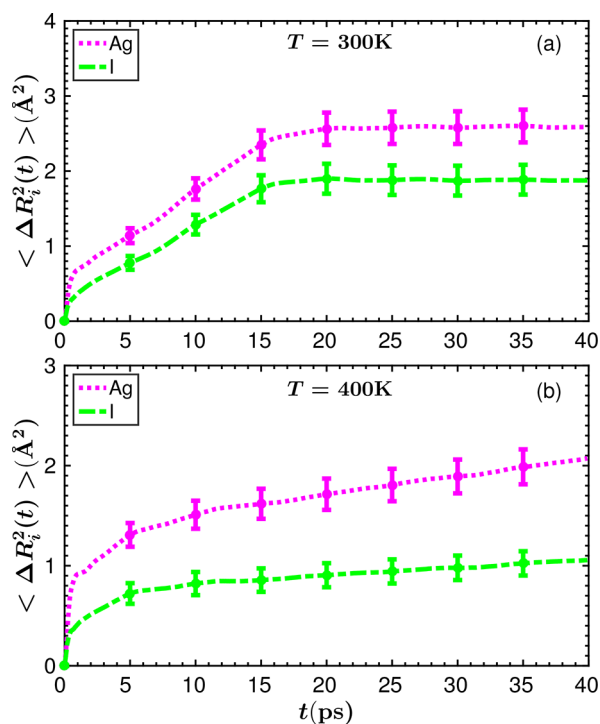


**Figure 13.** Mean squared displacement of AgI ( $\gamma$  phase) calculated with MD methods and considering a nondefective system ( $c_v = 0\%$ ) at  $\sigma_{xx} = \sigma_{yy} = 1$  GPa and  $T =$  (a) 300 and (b) 400 K conditions. Lines are guides to the eye.

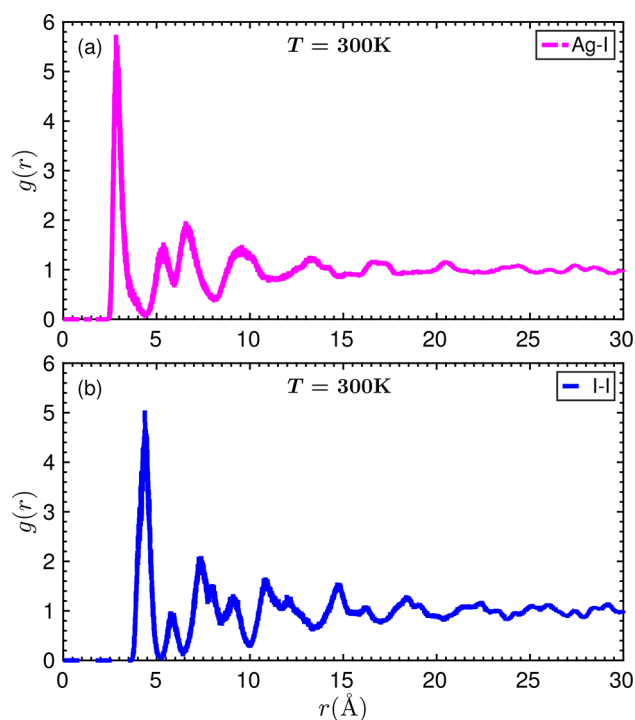


**Figure 14.** Radial pair distribution function of AgI ( $\gamma$  phase) calculated with MD methods and considering a nondefective system ( $c_v = 0\%$ ) at  $\sigma_{xx} = \sigma_{yy} = 1$  GPa, as obtained for (a) Ag–I pairs and (b) I–I pairs.

translational invariance in the crystal, in analogy to what is observed in glassy systems. The ionic density plots shown in Figures 15a–c clearly illustrate this effect in the  $\text{Ag}^+$  sublattice, as no ionic equilibrium positions or crystalline order can be

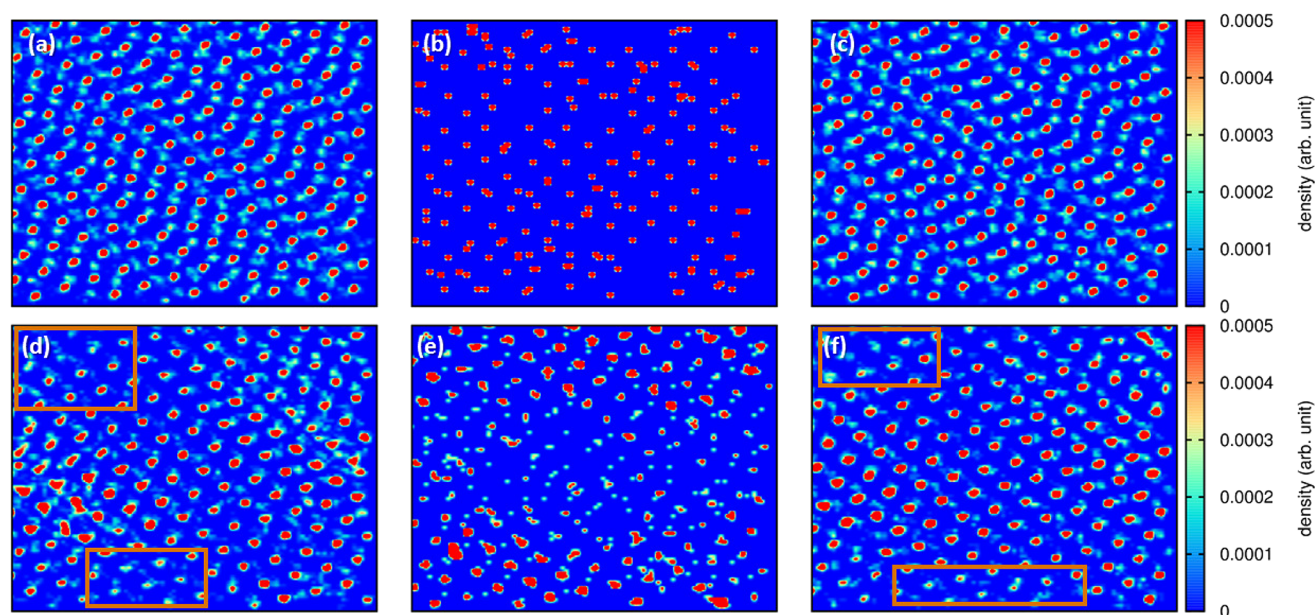


**Figure 15.** Silver density plots calculated in AgI ( $\gamma$  phase) with MD methods at  $\sigma_{xx} = \sigma_{yy} = 1$  GPa and  $T = 300$  K conditions. (a–c) Perfect system. (d–f) Defective system ( $c_v = 1\%$ ); regions containing vacancies are highlighted with orange boxes. For clarity purposes, the positions of  $\Gamma^-$  ions are not shown.

identified with precision in there (complementary plots of the corresponding intermediate scattering function<sup>32</sup> can be found in the [Supporting Information](#)).

Additionally, we performed an analysis of the vibrational phonon properties of strained AgI at zero temperature with first-principles methods (see [Section 2.2](#)). For an epitaxial strain of approximately  $-9\%$  (which corresponds to a biaxial compressive stress of approximately 2 GPa at  $T = 0$ ), we found an imaginary zone-boundary phonon eigenmode that is 2-fold degenerate and can be indexed in conventional reciprocal basis as  $X = (\frac{1}{2}, \frac{1}{2}, 0)$ . Imaginary phonon eigenmodes indicate the presence of structural instabilities in the crystal. The eigenvector of such an imaginary phonon eigenmode involves displacements of both  $\text{Ag}^+$  and  $\text{I}^-$  ions, which is consistent with what is observed in our finite-temperature simulations. Specifically, iodine ions are displaced along the Cartesian  $z$  direction, whereas silver ions are displaced along  $x$  or  $y$ . Although the strain–stress conditions at which this vibrational instability appears differ appreciably from those found in our  $T \neq 0$  simulations, we may interpret these *ab initio* results as further evidence of the occurrence of an order–disorder phase transition in  $\gamma$ -AgI induced by biaxial compressive stress (mind that thermal effects are completely disregarded in our zero-temperature vibrational analysis).

In [Figure 12](#), we also can appreciate the effects of vacancies on the superionic transition temperature of strained  $\gamma$ -AgI. At  $\sigma = 0$  conditions, it is found that a vacancy concentration of 1% induces a  $T_s$  reduction of about 100 K; this variation is considerably smaller than found, for instance, in  $\text{CaF}_2$  under similar conditions (see [Section 3.1](#)). When defective AgI is subjected to biaxial compressive stress, its superionic transition temperature first remains more or less constant up to  $\sigma_c \sim 0.6$  GPa and subsequently decreases monotonically under higher loads. As a result of such a steady reduction, we find that  $T_s$  reaches room temperature at  $\sigma = 1$  GPa (within our numerical uncertainty of  $\sim 50$  K). The cause of this systematic enhancement of ionic conductivity at  $\sigma_c < \sigma$  is, analogously

to what we found in the  $c_v = 0\%$  case, the occurrence of an order–disorder phase transition (as we verified through the analysis of MSD and  $g(r)$ 's profiles, not shown here). The disordered phase that is stabilized upon compressive biaxial stress is illustrated in [Figures 15d–f](#); there, we plot several representative  $\text{Ag}^+$  density maps in which, again, it is not possible to unequivocally identify periodic order. [Figures 15d–f](#) also show that the voids introduced by the vacancies become preferential interstitial sites.

It is worth emphasizing that the revealed order–disorder phase transition stands as the main cause of the  $\sigma$ -induced enhancement of ionic conductivity in  $\gamma$ -AgI. According to our simulations, the (pseudo) zincblende phase is not able to sustain superionicity by itself under specific biaxial compressive loads. This effect appears to be reminiscent of the superionic behavior observed in bulk AgI (which is of type-I<sup>1</sup>). It remains to be shown whether similar superionic phenomena as those reported here for  $\gamma$ -AgI under biaxial stress occur also in other families of type-I FIC (e.g.,  $\text{Ag}^+$  and  $\text{Cu}^+$  chalcogenides and halides).

#### 4. SUMMARY

In this work, we analyzed the effects of vacancies and biaxial stress on the ionic transport properties of three well-known families of FIC (namely, type-I, type-II, and Li-rich antiperovskite) using classical molecular dynamics and first-principles simulation methods. The main conclusion emerging from our study is that the combined action of point defects (created via irradiation methods, for instance, or naturally occurring in surfaces and interfaces) and biaxial stress (or, conversely, epitaxial strain) can be employed to effectively tune the critical transition temperature of superionic materials.

Specifically,  $\text{CaF}_2$  and  $\text{Li}_3\text{OCl}$  present a systematic reduction (increase) of  $T_s$  when subjected to tensile (compressive) biaxial stress. This behavior is related to the impact of biaxial stress on the formation energy of Frenkel pair defects, which in turn can be understood in terms of total volume changes. These

conclusions can be generalized to other type-II and akin FIC compounds in which the symmetry of the sublattices formed by the nondiffusive ions remain unaltered during the normal to superionic transformation. By contrast, superionicity in  $\gamma$ -AgI is enhanced through the application of biaxial compressive stresses when these are larger than a particular threshold value,  $\sigma_c$ . According to our calculations,  $\sigma_c$  depends strongly on the concentration of ionic vacancies. In this case, the observed enhancement of ionic conductivity is related to the triggering of a order–disorder phase transition, which opens up the necessary structural paths for ion migration. It remains to be confirmed whether similar behavior may also occur in other families of type-I fast-ion conductors under biaxial stress constraints.

Our findings show that a number of FIC with superionic transition temperatures close to room temperature (e.g.,  $\text{PbF}_2$ , halide perovskites, and  $\text{Ag}^+$  and  $\text{Cu}^+$  chalcogenides compounds) could become suitable materials for use in advanced energy applications (e.g., electrochemical batteries and solid-state cooling) via the combined action of biaxial stress and creation of ionic vacancies. Uniaxial stresses ( $\sigma_{xx} = \sigma_{yy} = 0$  and  $\sigma_{zz} \neq 0$ ) can be expected to produce ionic conductivity enhancement effects similar to those reported here because either compressive or tensile loads can also be achieved with them in practice. In view of the present great demand on energy materials, we encourage experimental searches to synthesize and gauge the potential of biaxially strained fast-ion conductors.

## ■ ASSOCIATED CONTENT

### Supporting Information

The Supporting Information is available free of charge on the ACS Publications website at DOI: 10.1021/acsami.7b11687.

Atomistic models of ionic diffusion in  $\text{CaF}_2$  and  $\text{Li}_3\text{OCl}$ , tests on the selected technical parameters in our simulations, ionic diffusion coefficients in  $\text{Li}_3\text{OCl}$  and  $\text{AgI}$  expressed as a function of ionic vacancy concentration and temperature, ionic coordination numbers in  $\text{AgI}$  calculated at different  $\sigma$ – $T$  conditions, and intermediate scattering functions of the mobile ionic species in  $\text{CaF}_2$ ,  $\text{Li}_3\text{OCl}$ , and  $\text{AgI}$  in the superionic state (PDF)

## ■ AUTHOR INFORMATION

### Corresponding Author

\*E-mail: c.cazorla@unsw.edu.au.

### ORCID

Claudio Cazorla: 0000-0002-6501-4513

### Notes

The authors declare no competing financial interest.

## ■ ACKNOWLEDGMENTS

This research was supported under the Australian Research Council's Future Fellowship funding scheme (Grant FT140100135). Computational resources and technical assistance were provided by the Australian Government and the Government of Western Australia through Magnus under the National Computational Merit Allocation Scheme and The Pawsey Supercomputing Centre.

## ■ REFERENCES

- (1) Hull, S. Superionics: Crystal Structures and Conduction Processes. *Rep. Prog. Phys.* **2004**, *67*, 1233–1314.
- (2) Wachsmann, E. D.; Lee, K. T. Lowering the Temperature of Solid Oxide Fuel Cells. *Science* **2011**, *334*, 935–939.
- (3) Kamaya, N.; Homma, K.; Yamakawa, Y.; Hirayama, M.; Kanno, R.; Yonemura, M.; Kamiyama, T.; Kato, Y.; Hama, S.; Kawamoto, K.; Mitsui, A. A Lithium Superionic Conductor. *Nat. Mater.* **2011**, *10*, 682–686.
- (4) Wang, Y.; Richards, W. D.; Ong, S. P.; Miara, L. J.; Kim, J. C.; Mo, Y.; Ceder, G. Design Principles for Solid-State Lithium Superionic Conductors. *Nat. Mater.* **2015**, *14*, 1026–1031.
- (5) Urban, A.; Seo, D.-H.; Ceder, G. Computational Understanding of Li-Ion Batteries. *NPJ. Comp. Mater.* **2016**, *2*, 16002.
- (6) Cazorla, C. In the Search of Novel Electrocaloric Materials: Fast-Ion Conductors. *Results Phys.* **2015**, *5*, 262–263.
- (7) Cazorla, C.; Errandonea, D. Giant Mechanocaloric Effects in Fluorite-Structured Superionic Materials. *Nano Lett.* **2016**, *16*, 3124–3129.
- (8) Shao, Z.; Haile, S. M. A High-Performance Cathode for the Next Generation of Solid-Oxide Fuel Cells. *Nature* **2004**, *431*, 170–173.
- (9) Sata, N.; Eberman, J.; Eberl, K.; Maier, J. Mesoscopic Fast Ion Conduction in Nanometre-Scale Planar Heterostructures. *Nature* **2000**, *408*, 946–949.
- (10) Garcia-Barriocanal, J.; Rivera-Calzada, A.; Varela, M.; Sefrioui, Z.; Iborra, E.; Leon, C.; Pennycook, S. J.; Santamaria, J. Colossal Ionic Conductivity at Interfaces of Epitaxial  $\text{ZrO}_2\text{:Y}_2\text{O}_3/\text{SrTiO}_3$  Heterostructures. *Science* **2008**, *321*, 676–680.
- (11) Deng, Z.; Radhakrishnan, B.; Ong, S. P. Rational Composition Optimisation of the Lithium-rich  $\text{Li}_3\text{OCl}_{1-x}\text{Br}_x$  Anti-Perovskite Superionic Conductors. *Chem. Mater.* **2015**, *27*, 3749–3755.
- (12) Richards, W. D.; Wang, Y.; Miara, L. J.; Kim, J. C.; Ceder, G. Design of  $\text{Li}_{1+2x}\text{Zn}_{1-x}\text{PS}_4$ , A New Lithium Ion Conductor. *Energy Environ. Sci.* **2016**, *9*, 3272–3278.
- (13) Cazorla, C.; Errandonea, D. Superionicity and Polymorphism in Calcium Fluoride at High Pressure. *Phys. Rev. Lett.* **2014**, *113*, 235902–235906.
- (14) Pennycook, T. J.; Beck, J. M.; Varga, K.; Varela, M.; Pennycook, S. J.; Pantelides, T. Origin of Colossal Ionic Conductivity in Oxide Multilayers: Interface Induced Sublattice Disorder. *Phys. Rev. Lett.* **2010**, *104*, 115901–115905.
- (15) Lee, J.; Pennycook, S. J.; Pantelides, S. T. Simultaneous Enhancement of Electronic and  $\text{Li}^+$  Ion Conductivity in  $\text{LiFePO}_4$ . *Appl. Phys. Lett.* **2012**, *101*, 033901–033904.
- (16) Pilvi, T.; Arstila, K.; Leskelä, M.; Ritala, M. Novel ALD Process for Depositing  $\text{CaF}_2$  Thin Films. *Chem. Mater.* **2007**, *19*, 3387–3392.
- (17) Kennedy, J. H. Thin Film Solid Electrolyte Systems. *Thin Solid Films* **1977**, *43*, 41–92.
- (18) Kumar, P. S.; Dayal, P. B.; Sunandana, C. S. On the Formation Mechanism of  $\gamma$ -AgI Thin Films. *Thin Solid Films* **1999**, *357*, 111–118.
- (19) Vetter, J.; Novak, P.; Wagner, M. R.; Veit, C.; Moller, K. C.; Besenhard, J. O.; Winter, M.; Wohlfahrt-Mehrens, M.; Vogler, C.; Hammouche, A. Ageing Mechanisms in Lithium-Ion Batteries. *J. Power Sources* **2005**, *147*, 269–281.
- (20) Wen, K.; Lv, W.; He, W. Interfacial Lattice-Strain Effects on Improving the Overall Performance of Micro-Solid Oxide Fuel Cells. *J. Mater. Chem. A* **2015**, *3*, 20031–20050.
- (21) Peng, L.; Zhu, Y.; Chen, D.; Ruoff, R. S.; Yu, G. Two-Dimensional Materials for Beyond-Lithium-Ion Batteries. *Adv. Ener. Mater.* **2016**, *6*, 1600025.
- (22) Shi, Y.; Bork, A. H.; Schweiger, S.; Rupp, L. M. The Effect of Mechanical Twisting on Oxygen Ionic Transport in Solid-State Energy Conversion Membranes. *Nat. Mater.* **2015**, *14*, 721–724.
- (23) Fluri, A.; Pergolesi, D.; Roddatis, V.; Wokaun, A.; Lippert, T. In Situ Stress Observation in Oxide Films and How Tensile Stress Influences Oxygen Ion Conduction. *Nat. Commun.* **2016**, *7*, 10692.
- (24) Rupp, J. L. M. Ionic Diffusion as a Matter of Lattice-Strain for Electroceramic Thin Films. *Solid State Ionics* **2012**, *207*, 1–70.

- (25) Lü, X.; Wu, G.; Howard, J. W.; Chen, A.; Zhao, Y.; Daemen, L. L.; Jia, Q. Li-Rich Anti-Perovskite  $\text{Li}_3\text{OCl}$  Films with Enhanced Ionic Conductivity. *Chem. Commun.* **2014**, *50*, 11520–11522.
- (26) Lü, X.; Howard, J. W.; Chen, A.; Zhu, J.; Li, S.; Wu, G.; Dowden, P.; Xu, H.; Zhao, Y.; Jia, Q. Antiperovskite  $\text{Li}_3\text{OCl}$  Superionic Conductor Films for Solid-State Li-ion Batteries. *Adv. Sci.* **2016**, *3*, 1500359–1500363.
- (27) Plimpton, S. J. Fast Parallel Algorithms for Short-Range Molecular Dynamics. *J. Comput. Phys.* **1995**, *117*, 1–19.
- (28) Cazorla, C.; Errandonea, D. High-Pressure, High-Temperature Phase Diagram of Calcium Fluoride from Classical Atomistic Simulations. *J. Phys. Chem. C* **2013**, *117*, 11292–11301.
- (29) Lu, Z.; Chen, C.; Baiyee, Z. M.; Chen, X.; Niu, C.; Ciucci, F. Defect Chemistry and Lithium Transport in  $\text{Li}_3\text{OCl}$  Anti-Perovskite Superionic Conductors. *Phys. Chem. Chem. Phys.* **2015**, *17*, 32547–32555.
- (30) Mouta, R.; Melo, M. A. B.; Diniz, E. M.; Paschoal, C. W. A. Concentration of Charge Carriers, Migration, and Stability in  $\text{Li}_3\text{OCl}$  Solid Electrolytes. *Chem. Mater.* **2014**, *26*, 7137–7144.
- (31) Vashishta, P.; Rahman, A. Ionic Motion in  $\alpha\text{-AgI}$ . *Phys. Rev. Lett.* **1978**, *40*, 1337–1340.
- (32) Gillan, M. J. The Simulation of Superionic Materials. *Physica B + C* **1985**, *131*, 157–174.
- (33) Wolf, M. L.; Walker, J. R.; Catlow, C. R. A. A Molecular Dynamics Simulation Study of the Superionic Conductor Lithium Nitride: I. *J. Phys. C: Solid State Phys.* **1984**, *17*, 6623–6634.
- (34) Kresse, G.; Furthmüller, J. Efficient Iterative Schemes for Ab Initio Total-Energy Calculations Using a Plane-Wave Basis Set. *Phys. Rev. B: Condens. Matter Mater. Phys.* **1996**, *54*, 11169–11186.
- (35) Perdew, J. P.; Burke, K.; Ernzerhof, M. Generalized Gradient Approximation Made Simple. *Phys. Rev. Lett.* **1996**, *77*, 3865–3868.
- (36) Blöchl, P. E. Projector Augmented-Wave Method. *Phys. Rev. B: Condens. Matter Mater. Phys.* **1994**, *50*, 17953–17979.
- (37) Kresse, G.; Furthmüller, J.; Hafner, J. Ab Initio Force Constant Approach to Phonon Dispersion Relations of Diamond and Graphite. *Europhys. Lett.* **1995**, *32*, 729–734.
- (38) Alfe, D. PHON: A Program to Calculate Phonons Using the Small Displacement Method. *Comput. Phys. Commun.* **2009**, *180*, 2622–2633.
- (39) Cazorla, C.; Íñiguez, J. Insights Into the Phase Diagram of Bismuth Ferrite from Quasiharmonic Free-Energy Calculations. *Phys. Rev. B: Condens. Matter Mater. Phys.* **2013**, *88*, 214430.
- (40) Parrinello, M.; Rahman, A.; Vashishta, P. Structural Transitions in Superionic Conductors. *Phys. Rev. Lett.* **1983**, *50*, 1073–1076.
- (41) Zimmer, F.; Ballone, P.; Maier, J.; Parrinello, M. Charge Carrier Interactions in Ionic Conductors: A Classical-Molecular Dynamics and Monte Carlo Study on  $\text{AgI}$ . *J. Chem. Phys.* **2000**, *112*, 6416–6422.
- (42) Keen, D. A.; Hull, S.; Hayes, W.; Gardner, N. J. G. Structural Evidence for a Fast-Ion Transition in the High-Pressure Rocksalt Phase of Silver Iodide. *Phys. Rev. Lett.* **1996**, *77*, 4914–4917.
- (43) Jalem, R.; Rushton, M. J. D.; Manalastas, W., Jr.; Nakayama, M.; Kasuga, T.; Kilner, J. A.; Grimes, R. W. Effects of Gallium Doping in Garnet-Type  $\text{Li}_7\text{La}_3\text{Zr}_2\text{O}_{12}$  Solid Electrolytes. *Chem. Mater.* **2015**, *27*, 2821–2831.
- (44) Gillan, M. J. Computer Simulation of Fast Ion Conductors. *Solid State Ionics* **1983**, *9*, 755–766.
- (45) Rix, S. Radiation-Induced Defects in Calcium Fluoride and Their Influence on Material Properties Under 193 nm Laser Irradiation. Ph.D. thesis, Johannes Gutenberg Universität, Mainz, 2011.
- (46) Goff, J. P.; Hayes, W.; Hull, S.; Hutchings, M. T. Neutron Powder Diffraction Study of the Fast-Ion Transition and Specific Heat Anomaly in  $\beta$ -Lead Fluoride. *J. Phys.: Condens. Matter* **1991**, *3*, 3677–3687.
- (47) Castiglione, M. J.; Madden, P. A. Fluoride Ion Disorder and Clustering in Superionic  $\text{PbF}_2$ . *J. Phys.: Condens. Matter* **2001**, *13*, 9963–9983.
- (48) Zhao, Y.; Daemen, L. L. Superionic Conductivity in Lithium-Rich Anti-Perovskites. *J. Am. Chem. Soc.* **2012**, *134*, 15042–15047.
- (49) Zhang, Y.; Zhao, Y.; Chen, C. Ab Initio Study of the Stabilities of and Mechanism of Superionic Transport in Lithium-Rich Antiperovskites. *Phys. Rev. B: Condens. Matter Mater. Phys.* **2013**, *87*, 134303.